INORGANIC CHEMISTRY
FRONTIERS

RESEARCH ARTICLE

View Article Online
View Journal | View Issue

Check for updates

Cite this: *Inorg. Chem. Front.*, 2024, **11**, 4711

Blue light-excited broadband NIR-II-emitting $Li_2ZnSn_3O_8$:Cr^{3+},Ni^{2+} phosphor for multifunctional optical applications†

Zhexuan Gao,[a] Yi Zhang,[a] Yinyan Li,[a] Shilong Zhao,[a] Peng Zhang,[a] Xiaolong Dong,[b] Degang Deng *[a] and Shiqing Xu*[a]

Received 9th April 2024,
Accepted 30th May 2024

DOI: 10.1039/d4qi00896k

rsc.li/frontiers-inorganic

The second near-infrared window (NIR-II, 1000–1700 nm) emitting phosphor is a key component for the phosphor-converted light-emitting diode (pc-LED), which has garnered significant attention. However, it remains a major challenge to discover efficient NIR-II broadband phosphors that can be excited by blue LEDs. Herein, Cr^{3+} and Ni^{2+} ions were co-doped into the $Li_2ZnSn_3O_8$ (LZSO) host. LZSO:Cr^{3+},Ni^{2+} phosphor achieves a broadband NIR-II emission peak at 1465 nm with a large full width at half maximum (FWHM) of 300 nm and internal quantum efficiency (IQE) of 43.31% under excitation at 426 nm because of the efficient energy transfer (ET) from Cr^{3+} to Ni^{2+}. In addition, a dual-emissive doped phosphor across the NIR-I (700–1000 nm) and NIR-II regions with a higher sensitivity at physiological temperatures was obtained. The relative sensitivity value (S_r) reaches 1.44% K^{-1} at 293 K, indicating that the LZSO:Cr^{3+},Ni^{2+} phosphor is a potential candidate for NIR optical thermometers in biotechnological applications. The manufactured NIR-II pc LED provides a radiative flux of 8.26 mW with a photoelectric conversion efficiency of 2.71% at a drive current of 100 mA and has promising potential in night vision, medical imaging, and spectral analysis applications.

1 Introduction

NIR light sources have various applications in non-invasive biological imaging, optical communication, health monitoring, and night vision.[1–4] The pc-LED based on energy down-conversion technology serves as a novel type of NIR light source, offering advantages such as low cost, high efficiency, portability, and long lifetime, which is also known as a replacement for traditional NIR light sources such as incandescent lamps, tungsten halogen lamps, and NIR LEDs.[5,6] A reliable method to obtain this NIR light source is by combining NIR phosphor with inexpensive high-efficiency blue light chips. The NIR phosphor determines the characteristics of NIR pc-LED, including the emission peak, FWHM, and luminous efficiency. Typically, the emission spectra of NIR phosphors are located in NIR-I and NIR-II regions.[7,8] In comparison to NIR-I, NIR-II has less background interference, less tissue scattering, deeper tissue penetration depth, and high imaging contrast.[9,10] In addition, dipole moments and bond anharmonicities play a significant role in the typical NIR absorptions that arise from overtones and combinations of fundamental vibrations. However, the behavior of C–H, O–H, N–H, and S–H bonds varies in different substances and corresponds to significant absorptions mainly located in the broad wavelength range above 1000 nm.[11–13] Therefore, NIR-II light is more suitable for achieving promising night vision, biomedical and spectral analysis applications.

Cr^{3+} with a $3d^3$ electron configuration typically exhibits intrinsic broad emission when entering octahedral sites, which has attracted widespread attention.[14–16] In recent years, a group of excellent NIR emission performance Cr^{3+}-doped phosphors excited by blue light has been reported, such as $Ba_5La_3MgAl_3O_{15}$:Cr^{3+} (λ_{em} = 925 nm, IQE = 66%), Ga_2GeO_5:Cr^{3+} (λ_{em} = 923 nm, IQE = 71.25%), $NaInSi_2O_6$:Cr^{3+} (λ_{em} = 936 nm, IQE = 68.9%), and $LiScGeO_4$:Cr^{3+}(λ_{em} = 1120 nm, IQE = 26%).[5,17–19] Nevertheless, the maximum peak position at around 1000 nm and the limited spectral bandwidth are insufficient to meet various practical application requirements. Co-doping of Yb^{3+} for ET from Cr^{3+} to increase spectral bandwidth and improve NIR emission performance is a good choice, such as $KScP_2O_7$:Cr^{3+},Yb^{3+}, $CaZnGe_2O_6$:Cr^{3+},Yb^{3+}, $LiScP_2O_7$:Cr^{3+},Yb^{3+}, $LiIn_2SbO_6$:Cr^{3+},Yb^{3+}, $LiGaP_2O_7$:Cr^{3+},Yb^{3+},

---

[a] *Key Laboratory of Rare Earth Optoelectronic Materials and Devices of Zhejiang Province, Institute of Optoelectronic Materials and Devices, China Jiliang University, Hangzhou 310018, China. E-mail: dengdegang@cjlu.edu.cn; Fax: +86-571-86835781; Tel: +86-571-86835781*

[b] *Fujian Institute of Metrology, Fuzhou,350003, China*

† Electronic supplementary information (ESI) available. See DOI: **https://doi.org/10.1039/d4qi00896k**

$Lu_{0.2}Sc_{0.8}BO_3$:Cr^{3+},Yb^{3+}, and $Y_3Ga_5O_{12}$:Cr^{3+},Yb^{3+}.[12,20–25] However, considering the emission characteristics of Yb^{3+} ions, their emission wavelength are still difficult to embrace the NIR-II region.[26] Therefore, exploring novel infrared phosphors with efficient emission in the NIR-II region by doping with other optically active ions is necessary.

Ni^{2+}-activated phosphors display broadband emission in the NIR-II range. Unfortunately, these phosphors are typically excited by UV light, which has drawbacks of weak blue light absorption and low efficiency (IQE, EQE < 10%).[27–29] To address this issue, Cr^{3+} can be introduced as a sensitizer in the material system to effectively transfer energy to Ni^{2+}. In consideration of the broad absorption band of Cr^{3+} in the blue region and the perfect overlap between the absorption of Ni^{2+} and the emission of Cr^{3+}. Therefore, when Cr^{3+} and Ni^{2+} are simultaneously introduced into a suitable host, the emission in the NIR-II range of Ni^{2+} can be achieved through sensitization by Cr^{3+} excited by blue LEDs.[30]

Furthermore, the progress of dual-emissive materials for thermometers relies on visible light (VIS). The optical thermometer emission wavelength in the biological window (NIR-I, NIR-II) could make it suitable for applications such as biomedical thermal imaging or more sensitive temperature sensing for the development and application of biotechnology.[31,32] However, the progress of thermometers based on dual-emissive materials that originate from NIR-I and NIR-II light has been minimal. Accordingly, developing dual-emissive doped phosphors that cover both NIR I and NIR II regions and have higher sensitivity at physiological temperatures remains a challenge.

Herein, we report a blue LED-excited and highly efficient NIR-II phosphor LZSO:Cr^{3+},Ni^{2+}. The photoluminescence spectra, luminescence decay curves, ET efficiency, quantum efficiency, and thermal stability of LZSO:$0.03Cr^{3+}$,$0.03Ni^{2+}$ phosphor were investigated. A fabricated NIR-II pc-LED was applied in night vision, biomedical imaging, and spectroscopic analysis fields. Furthermore, the broadband NIR dual-emissive properties of LZSO:$0.03Cr^{3+}$,$0.03Ni^{2+}$ are noteworthy and provide insights for optical thermometers applicable in biotechnology.

2 Experimental

2.1 Materials and synthesis

Reagents: lithium carbonate (Li_2CO_3, 99.99%), zinc oxide (ZnO, 99.99%), stannic oxide (SnO_2, 99.99%), chromium sesquioxide (Cr_2O_3, 99.95%), and niobium pentaoxide (NiO, 99.99%) were supplied by Aladdin Reagent Co., Ltd.

Synthesis: stoichiometric raw materials were weighed based on stoichiometric ratios. The mixtures were combined completely homogeneous in an agate mortar. Subsequently, they were placed in a muffle furnace sintered at 1200 °C for 3 h, and the heating rate was maintained at 6.5 °C min^{-1}, which contributes to a full reaction. Then, the samples were cooled naturally to room temperature and ground with the aim of subsequent testing.

2.2 Characterization

Power X-ray diffraction (XRD) patterns of the phosphor were acquired by employing Bruker Axs D2 PHASER diffractometer with Cu Kα radiation (λ = 0.15405 nm) at 30 kV and 10 mA. Rietveld refinement was performed using the software the General Structural Analysis System (GASA). The field-emission scanning electron microscopy (SEM) and energy-dispersive spectroscopy (EDS) were performed using the HITACHI, SU8010, instrument, Japan. Field-emission transmission electron microscopy (TEM) was conducted at an acceleration voltage of 200 kV (FEI, SU 8010, America). The diffuse reflectance spectra (DRS) of the phosphors were collected using an ultraviolet spectrophotometer (Agilent Cay 5000, America) with $BaSO_4$ as a standard. The fluorescence decay curve was obtained using a 460 nm LED pulse Nd: YAG laser with a fl3-211 fluorescence spectrophotometer (HORIBA, JOBIN YVON, France). The photoluminescence (PL) and photoluminescence excitation (PLE) spectra were recorded on a modular fluorescence spectrometer (HORIBA, Quanta Master 8000, Canada). The corresponding temperature-dependence PL spectra were recorded on the same spectrophotometer equipped with a TAP-02 high-temperature fluorescence instrument (Tian Jin Orient – KOJI Instrument Co., Ltd). A quantum yield (QY) measurement system (Hamamatsu, Quantaurus-QY plus C13684-01) was used to measure the internal and external quantum efficiency (IQE, EQE); the electroluminescence (EL) spectra were collected using a FL3-211 fluorescence spectrophotometer (HORIBA, JOBIN YVON, France). An LED photoelectric test system (HAAS-2000, EVER FINE) was employed to analyze the performance of the fabricated LED. Visible and NIR-II photographs were captured by an industrial camera (EOS R50, Canon, China) and an NIR-II camera (Raptor Owl 640 S).

2.3 Fabrication of the pc-LED device

The optimal LZSO:$0.03Cr^{3+}$,$0.03Ni^{2+}$ phosphor was used to package the NIR-II pc-LED, which was sufficiently mixed with glue A and glue B in conformity with the weight ratio of 1 : 1 on a blue chip (460 nm, 3 W) and then cured at 150 °C for 3 h.

3 Results and discussion

It is reported that LZSO in the orthorhombic system with space group *Cmc*21 (No. 36), as shown in Fig. 1a.[33] Li^+ ions are coordinated to six oxygen ions to form [$Li1O_6$], [$Li2O_6$] octahedra and four oxygen ions to form [$Li3O_6$], [$Li4O_6$] tetrahedra. Sn^{4+} ions have five different crystallographic sites coordinated with six oxygen ions to form five different kinds of SnO6 octahedra. While the Zn^{2+} ion is linked to four oxygen ions to form two [ZnO_4] tetrahedra. These coordinated polyhedra are orderly connected to form the LZSO unit. Fig. 1b shows XRD patterns of the representative LZSO, LZSO:$0.03Cr^{3+}$,

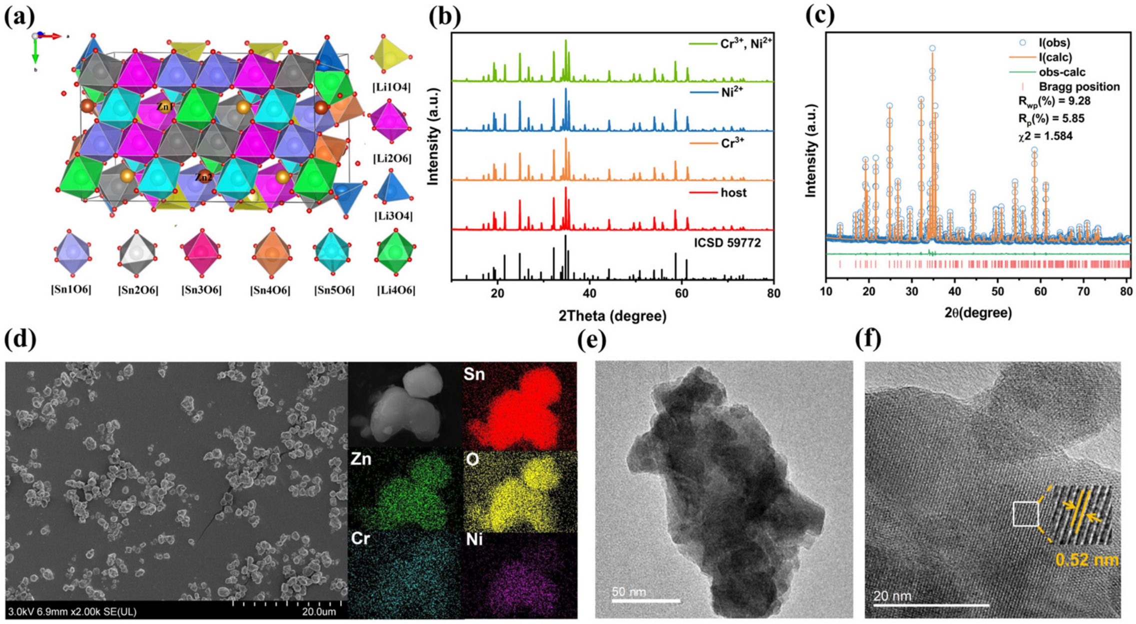

Fig. 1 (a) Crystal structure of LZSO. (b) XRD patterns of LZSO, LZSO:0.03Cr^{3+}, LZSO:0.03Ni^{2+}, and LZSO:0.03Cr^{3+},0.03Ni^{2+} samples. (c) Rietveld refinements of LZSO. (d) SEM and EDS mapping images of LZSO:0.03Cr^{3+},0.03Ni^{2+}. (e and f) TEM and HR-TEM of LZSO:0.03Cr^{3+},0.03Ni^{2+}.

LZSO:0.03Ni^{2+}, and LZSO:0.03Cr^{3+},0.03Ni^{2+} samples, as well as the XRD patterns of LZSO:xCr^{3+} and LZSO:0.03Cr^{3+},yNi^{2+} ($0.005 \leq x \leq 0.07$, $0.003 \leq y \leq 0.07$) phosphors (Fig. S1, ESI†). All diffraction peaks agree with the standard phase $Li_2ZnSn_3O_8$ in the Inorganic Crystal Structure Database (ICSD: 59772), demonstrating that the introduction of Cr^{3+} and Ni^{2+} dopants does not generate impurity phases. Considering that the valence and ionic radius of Cr^{3+} (coordination number, CN = 6, r = 0.615 Å) are very close to those of Sn^{4+} (CN = 6, r = 0.69 Å), the Cr^{3+} dopant prefers to substitute the Sn^{4+} ions in the LZSO host. From the perspective of charge balance, the substitution of Ni^{2+} (CN = 6, r = 0.69 Å) for two different Li^{+} (CN = 6, r = 0.76 Å) can avoid imbalance. Detailed crystallographic information was obtained by Rietveld's refinement of the XRD pattern of the prepared sample. It can be seen from Fig. 1c that the refined result of LZSO with R_p = 5.85%, R_{wp} = 9.28%, χ^2 = 1.584. The refinement result demonstrates reliable results and phase purity. The specific crystallographic data and the atomic positions of LZSO are listed in Tables S1 and S2† respectively. In addition, the morphology and elemental mapping distribution of the obtained phosphors were characterized from SEM images and EDS of LZSO:0.03Cr^{3+},0.03Ni^{2+} phosphors, as shown in Fig. 1d. The SEM image indicates the irregular morphology of the synthesized LZSO:0.03Cr^{3+},0.03Ni^{2+} phosphor. The smooth surface of the particles also indicates its high crystallinity. The EDS reveals the existence of Zn, Sn, O, and Cr, Ni elements in the LZSO:0.03Cr^{3+},0.03Ni^{2+} phosphor. The atomic percentages of Ni, Zn, Sn, Cr, and O in LZSO:0.03Cr^{3+},0.03Ni^{2+} were determined as 0.40%, 9.34%, 31.90%, 0.34% and 58.02% (Fig. S2†), respectively. However, the absence of Li is due to its low atomic number. The results approach an actual chemical formula of $Li_{1.97}Ni_{0.03}ZnSn_3Cr_{0.03}O_8$ (the atomic percentages neglecting Li are 0.25%, 8.31%, 24.69%, 0.25%, and 66.5%, respectively). Furthermore, TEM and HR-TEM images of LZSO:0.03Cr^{3+},0.03Ni^{2+} are displayed in Fig. 1e. The lattice fringes are clearly visible, and an estimated crystal plane spacing of 0.52 nm matches well with the (020) plane. These results confirm the good crystallinity of the synthesized phosphors.

The PL and PLE spectra of LZSO:0.03Cr^{3+}, LZSO:0.03Ni^{2+}, and LZSO:0.03Cr^{3+},0.03Ni^{2+} are presented in Fig. 2a. The broadband of LZSO:0.03Cr^{3+}, which peaks at 959 nm and spans a range of 700 to 1300 nm with a FWHM of 176 nm, is caused by the spin-allowed $^4T_2 \rightarrow {}^4A_2$ transition of Cr^{3+} ions when excited at 426 nm. Under the monitoring at 959 nm emission, the sample exhibits a wide excitation band from ultraviolet to red light, with the peak located in the blue light region, indicating that the LZSO:0.03Cr^{3+} phosphor can be effectively excited by the blue light chip. The excitation band centered at 288 nm could arise from charge transfer between the O ligand and the central Sn atom in the SnO6 octahedral group, while the excitation bands at 350, 426, 617 and 676 nm are ascribed to the $^4A_2 \rightarrow {}^4T_1$ (^{4}P), $^4A_2 \rightarrow {}^4T_1$ (^{4}F), $^4A_2 \rightarrow {}^4T_2$ (^{4}F) and $^4A_2 \rightarrow {}^2E(^2G)$ transitions of Cr^{3+} ions, respectively.[34,35] For LZSO:0.03Ni^{2+} phosphor, a broad emission centered at 1465 nm ranging from 1200–1750 nm (FWHM = 300 nm) was observed under excitation at 400 nm, derived from the $^3T_2 \rightarrow {}^3A_2$ transition of Ni^{2+} ions. At the same time, the sample has four peaks at 400, 426, 623, and 676 nm consisting of a continuous PLE spectrum monitored at 1465 nm, which originated from the $^3A_2$ (^{3}F) $\rightarrow$ $^3T_1$ (^{3}P), $^3A_2$ (^{3}F) $\rightarrow$ $^1T_2$ (^{1}D),

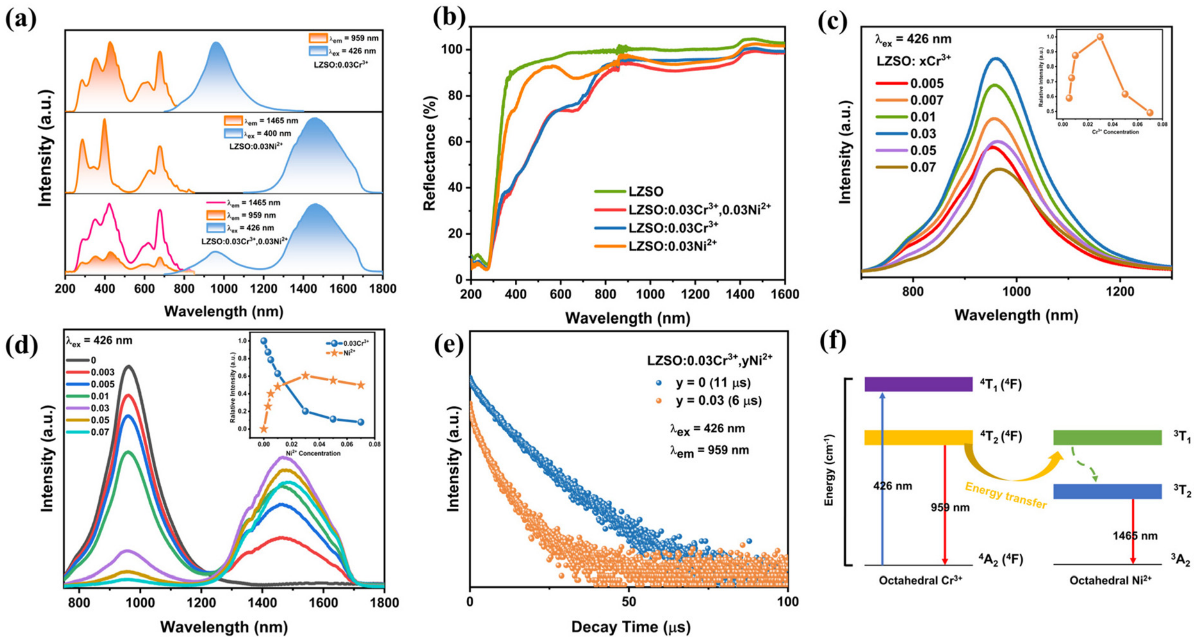

Fig. 2 (a)PLE and PL spectra of the LZSO:0.03Cr^{3+}, LZSO:0.03Ni^{2+}, and LZSO:0.03Cr^{3+},0.03Ni^{2+} phosphors. (b) DRS of LZSO, LZSO:0.03Cr^{3+}, LZSO:0.03Ni^{2+} and LZSO:0.03Cr^{3+},0.03Ni^{2+} phosphors. (c) PL spectra of LZSO:$x$$Cr^{3+}$ (x = 0.005–0.07), the inset depicts the dependence of PL intensity on the Cr^{3+} doping concentration. (d) PL spectra of LZSO:0.03Cr^{3+},$y$$Ni^{2+}$ (y = 0.003–0.07), the inset shows the PL intensity of the two emission bands with an increase of Ni^{2+} concentration. (e) Lifetime decay curves of Cr^{3+} in the LZSO:0.03Cr^{3+} and LZSO:0.03Cr^{3+},0.03Ni^{2+} samples. (f) The schematic diagram of the energy transfer process.

$^3A_2$ (^3F) → $^3T_1$ (^3F) and $^3A_2$(^3F) → ^1E(^1D) transitions of Ni^{2+} ions, respectively.[36] The LZSO:0.03Cr^{3+},0.03Ni^{2+} phosphor has two broad emission bands corresponding to the $^4T_2 \rightarrow {}^4A_2$ transition of Cr^{3+} and the $^3T_2 \rightarrow {}^3A_2$ transition of Ni^{2+} excited by 426 nm blue light. The PLE spectra of the LZSO:0.03Cr^{3+},0.03Ni^{2+} monitored at 959 and 1465 nm are similar to those of LZSO:0.03Cr^{3+}, indicating the ET from Cr^{3+} to Ni^{2+}. Compared to Ni^{2+} single-doped phosphor, which cannot be effectively excited by blue light irradiation, the co-doped Cr^{3+}, Ni^{2+} phosphor greatly broadens the excitation spectral range, especially in the blue light region, solving the problem of inefficient excitation of Ni^{2+} activator by blue light.

The DRS of LZSO:0.03Cr^{3+}, LZSO:0.03Ni^{2+}, and LZSO:0.03Cr^{3+},0.03Ni^{2+} samples correspond well with their respective PLE spectra (Fig. 2b). Moreover, no characteristic absorption band of Cr^{4+} around 1000 nm was observed in the LZSO:0.03Cr^{3+} sample, indicating that the emission center is Cr^{3+} ions rather than Cr^{4+}.[37] Meanwhile, the PL spectrum of LZSO:0.03Cr^{3+} and the PLE spectrum of LZSO:0.03Ni^{2+} show a significant overlap, as shown in Fig. S3,† demonstrating that the ET between Cr^{3+} and Ni^{2+} is possible. The Tanabe–Sugano diagrams demonstrate the splitting degree of the Cr^{3+} and Ni^{2+} ions located in octahedral coordination are presented in Fig. S4.† The online calculation program developed by Song *et al.* was used to calculate the D_q/B values related to the matrix for the $3d^3$ electronic configuration of Cr^{3+}.[38] The calculated intersection points for the ^2E and $^4T_2$ levels were found to be at 1.94, with the sample's D_q/B value at 2.13, close to the intersection point value. The crystal field strength in octahedrally coordinated approximation of Ni^{2+} can be calculated using eqn (S1) and (S2).† Consequently, the D_q/B value for Ni^{2+} can be given as 1.09. This indicates that the host provides a relatively weak crystal field for Ni^{2+} (D_q/B < 1.8). When Ni^{2+} ions are in a weak octahedral crystal field, they usually exhibit a broad emission band.[36]

The PL spectra of LZSO:$x$$Cr^{3+}$ (x = 0.005–0.07) phosphors under 426 nm excitation are shown in Fig. 2c. The highest PL intensity was obtained at x = 0.03, as shown in the inset of Fig. 2c. As the possibility of nonradiative transitions between Cr^{3+} ions increases, quenching will occur beyond this concentration.[39] Fig. 2d presents the PL spectra of LZSO:0.03Cr^{3+}, $y$$Ni^{2+}$ (y = 0.003–0.07) under 426 nm excitation. The inset illustrates the relative PL intensity of Cr^{3+} and Ni^{2+} in the LZSO:0.03Cr^{3+},$y$$Ni^{2+}$ system. The PL intensity of Cr^{3+} monotonically decreases with increasing Ni^{2+} concentration, while the emission intensity of Ni^{2+} is correspondingly enhanced and then declines. When y is 0.03, the PL intensity of Ni^{2+} is strongest owing to the concentration quenching effect. According to the PL intensity, the efficiency (η_{ET}) from Cr^{3+} to Ni^{2+} is obtained:[40]

$$\eta_{\mathrm{ET}} = 1 - \frac{I_{\mathrm{Cr,Ni}}}{I_{\mathrm{Cr}}} \tag{1}$$

where $I_{\mathrm{Cr,Ni}}$ and I_{Cr} represent the PL intensity of 0.03Cr^{3+} doped with and without Ni^{2+}, respectively. It can be found the date in Fig. S5† that the η_{ET} value increases continuously with the Ni^{2+} content increasing. When the Ni^{2+} concentration is 0.03, the η_{ET} value reaches as high as 78.95%. The observation of a noticeable red shift in the Ni^{2+} emission band can be attributed to the change in D_q around the Ni^{2+} ion. The value of D_q can be evaluated through the following equation:[2,41]

$$D_q = \frac{ze^2r^4}{6R^5} \tag{2}$$

where R stands for the distance between the central ion and the ligands, z means the charge of the anion, e and r present the charge of the electron and the radius of the activator. When Ni^{2+} ions (CN = 6, r = 0.69 Å) were doped into the LZSO host, it tends to occupy the larger Li^+ sites (CN = 6, r = 0.76 Å). With increasing Ni^{2+} doping concentration, the crystal field strength becomes weaker, resulting in a red shift of the emission peak. Furthermore, the absolute quantum yield of the LZSO:0.03Cr^{3+},0.03Ni^{2+} phosphor was determined using an integrating sphere. Moreover, the absolute quantum yield of the LZSO:0.03Cr^{3+},0.03Ni^{2+} phosphor in the NIR-II region was determined using an integrating sphere. As depicted in Fig. S6,† the measurement range of the NIR detector is limited (maximum ≈ 1688 nm), so the entire PL spectrum in the NIR-II region cannot be detected. Taking into account the 2.12% unmeasured portion, the actual IQE/EQE of the phosphor ranging from 1200 to 1750 nm under 426 nm laser excitation is calculated as 43.31%/18.24%. The optical performance comparison of LZSO:0.03Cr^{3+},0.03Ni^{2+} with previously reported NIR phosphors, is listed in Table S2.† Fig. 2f depicts the decay curves monitored at 959 nm under 426 nm excitation for LZSO:0.03Cr^{3+} and LZSO:0.03Cr^{3+},0.03Ni^{2+}. The decay curve of Cr^{3+} can be fitted using the double exponential function:[7,42]

$$I = I_0 + A_1\exp(-t/\tau_1) + A_2\exp(-t/\tau_2) \tag{3}$$

where I and I_0 belong to the PL intensities at times t and t = 0, respectively, t is time, A_1 and A_2 are corresponding fitting constants, τ_1 and τ_2 represent two different lifetimes of the exponential components. The following equations are used to estimate the average lifetime (τ^*) and ET efficiency (η'_{ET}):[6,43]

$$\tau_{Cr,Ni} = \frac{A_1{\tau_1}^2 + A_2{\tau_2}^2}{A_1\tau_1 + A_2\tau_2} \tag{4}$$

$$\eta'_{ET} = 1 - \frac{\tau_{Cr,Ni}}{\tau_{Cr}} \tag{5}$$

where $\tau_{Cr,Ni}$ and τ_{Cr} represent the decay times of Cr^{3+} with and without Ni^{2+}, respectively. Typically, two different lifetimes are observed. As the Ni^{2+} concentration increases from 0 to 0.03, the lifetime of Cr^{3+} decreases from 11 μs to 6 μs, confirming the ET from Cr^{3+} ions to Ni^{2+} ions. The calculated η'_{ET} for LZSO:0.03Cr^{3+},0.03Ni^{2+} is 45.46%, which differs significantly from the ET efficiency calculated based on PL intensity. Due to the rapid ET between the recent donor–acceptor pairs, we always neglect the fast ET component between the nearest neighbor Ni^{2+} and Cr^{3+} in the lifetime measurements. Therefore, the obtained ET efficiency is lower than the actual value. Given that the PL intensity of LZSO:0.03Cr^{3+},0.03Ni^{2+} remains unchanged in comparison to that of LZSO:0.03Ni^{2+}, the decline in Cr^{3+} emission can be attributed exclusively to ET towards Ni^{2+}, rather than other nonradiative relaxation transitions. Hence, estimating the change in the emission intensity provides a more accurate estimation of ET efficiency.[44] This phenomenon also occurs in Sr_2GaTaO_6:Cr^{3+},Ni^{2+} and other ET systems of $Cr^{3+} \rightarrow Yb^{3+}$, Ce^{3+}/$Eu^{2+} \rightarrow Mn^{2+}$.[44–46] The ET process from Cr^{3+} to Ni^{2+} is shown in Fig. 2f. Cr^{3+} ions are excited from the ground state $^4A_2$ to the $^4T_1(F)$ level by blue light at 426 nm firstly, followed by non-radiative relaxation to the $^4T_2(F)$ state. Some electrons undergo radiative transitions to the $^4A_2$ ground state, resulting in broadband emission between 700 and 1300 nm. These electrons are transferred to the neighboring Ni^{2+} ions in their $^3T_1$ excited state through the energy transfer processes. The subsequent $^3T_2 \rightarrow {}^3A_2$ transition leads to broadband emission centered at 1465 nm.

We also investigated the thermal properties of the LZSO:0.03Cr^{3+},0.03Ni^{2+} phosphor. Fig. 3a presents the temperature-dependent PL spectra of LZSO:0.03Cr^{3+},0.03Ni^{2+} upon 426 nm excitation. The emissions of both Cr^{3+} and Ni^{2+} decrease with increasing temperature. The relative PL intensity of Cr^{3+} can maintain 75.34% of its initial intensity at room temperature when the temperature is elevated from 303 to 373 K, while Ni^{2+} remains at 30.14% with increasing temperature. Temperature-dependent emission spectra and relative intensity of LZSO:Ni^{2+} are shown in Fig. S7.† The emission intensity of LZSO:Ni^{2+} is maintained at 27.63% at 373 K compared to that at 293 K. Thus, the thermal stability is improved with the introduction of Cr^{3+}. Generally speaking, the thermal quenching of Cr^{3+} and Ni^{2+} can occur through non-radiative transitions stemming from the crossing of excited state and ground state parabolas in the configurational coordination model (Fig. S8†).[47] The longer emission wavelength of the Ni^{2+} ion indicates a narrower band gap, which leads to a more severe thermal quenching effect.[26] The FWHM values of Cr^{3+} and Ni^{2+} in Fig. S9† extend from 498 and 317 to 960 nm and 655 nm, respectively, resulting from the increased electron–phonon coupling at high temperatures.[24] Meanwhile, the peak position of the PL spectra remains almost constant The emission-integrated intensity histogram of Cr^{3+} and Ni^{2+} ions is shown in Fig. 3c. The emissions of Cr^{3+} and Ni^{2+} ions exhibit different responses with increasing temperature in the range of 293–423 K, which especially shows significant changes in the physiological temperature range (293–323 K) and cover a biological window, indicating its potential application in biomedical research. In general, the fluorescence intensity ratio (FIR) represents the temperature more accurately. FIR is based on the integral intensity of each emission peak, which denotes the ratio of luminescence intensities between two different emission wavelengths under the same excitation wavelength.[43,48] To study the temperature sensing performance, the following equation can represent the relationship between FIR ($I_{959\ nm}/I_{1465\ nm}$) and temperature:[31]

$$\mathrm{FIR} = \frac{I_{\mathrm{low}}}{I_{\mathrm{high}}} = \frac{\int_{1200}^{1750} I(\lambda, T)\mathrm{d}\lambda}{\int_{750}^{1200} I(\lambda, T)\mathrm{d}\lambda} \tag{6}$$

Fig. 3d indicates the FIR datapoints fitted using eqn (6), which can be fitted by the $\mathrm{FIR} = 5.44\exp\left(-\frac{867}{T}\right) - 0.08$. The

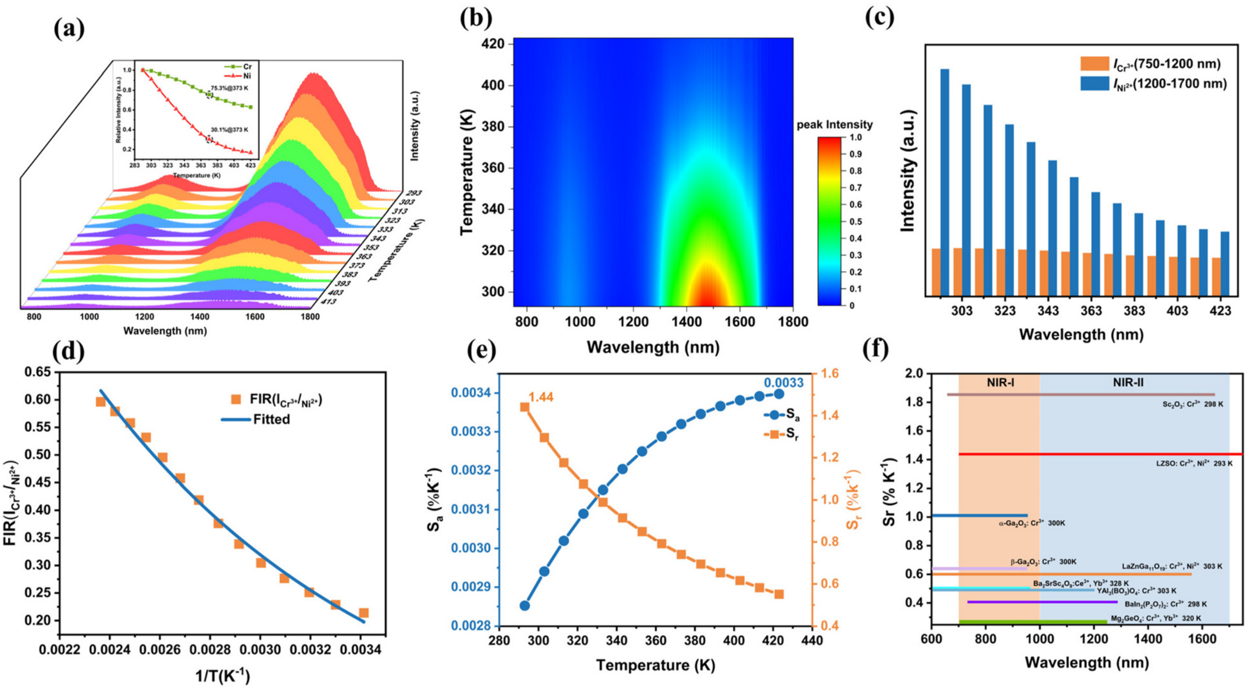

Fig. 3 (a and b) Temperature dependence of the PL spectra of LZSO:0.03Cr^{3+},0.03Ni^{2+}. The inset shows the intensity curves of different emission bands as a function of temperature. (c) Temperature-dependent histogram of the PL intensity for Cr^{3+} and Ni^{2+} of LZSO:0.03Cr^{3+},0.03Ni^{2+} (d) ($I_{959\ nm}/I_{1465\ nm}$) as functions of temperature. (e) Calculated S_a and S_r values. (f) S_r values at the physiological temperatures and NIR emission range of LZSO:Cr^{3+},Ni^{2+}, compared to other NIR optical thermometers under blue light excited, such as $LaZnGa_{11}O_9$:Cr^{3+},Ni^{2+}, α-Ga_2O_3:Cr^{3+}, β-Ga_2O_3:Cr^{3+}, $Ba_2SrSc_4O_9$:Ce^{3+},Yb^{3+}, $YScGaSbO_7$:Cr^{3+}, $YAl_3(BO_3)O_4$:Cr^{3+}, Mg_2GeO_4:Cr^{3+},Yb^{3+}, $BaIn_2(P_2O_7)_2$:Cr^{3+}, Sc_2O_3:Cr^{3+}.[2,31,42,50–53]

following equations outline the fitting curves for the optical thermometer's absolute sensitivity (S_a) and its relative sensitivity (S_r):[49]

$$S_a = \left|\frac{\partial \mathrm{FIR}}{\partial T}\right| \tag{7}$$

$$S_r = 100\% \times \left|\frac{1}{\mathrm{FIR}}\frac{\partial \mathrm{FIR}}{\partial T}\right| \tag{8}$$

The values of S_a and S_r at different temperatures (298–423 K) are shown in Fig. 3e. S_a reaches its peak value of 0.34% K^{-1} at 423 K. The S_r value decreases from 1.44% K^{-1} to 1.08% K^{-1} as the physiological temperature range increases from 293 K to 323 K. Fig. 3f provides a performance comparison of LZSO:0.03Cr^{3+},0.03Ni^{2+} and a number of reported NIR optical thermometers at physiological temperatures. It is worth noting that LZSO:0.03Cr^{3+},0.03Ni^{2+} exhibits a high S_r value with an ultra-broadband spanning from 700 to 1750 nm, covering the NIR-I and NIR-II windows. As a consequence, these results demonstrate that the LZSO:0.03Cr^{3+},0.03Ni^{2+} system has great potential in the biological application field of optical thermometers.

Fig. 4a displays the EL spectra of the prepared NIR-II pc-LED under different driving currents. It is observed that all the EL spectra consist of a dominant NIR-II broadband NIR emission at ≈1465 nm and a weak blue emission ≈at 460 nm, indicating that LZSO:Cr^{3+},Ni^{2+} phosphors can effectively convert

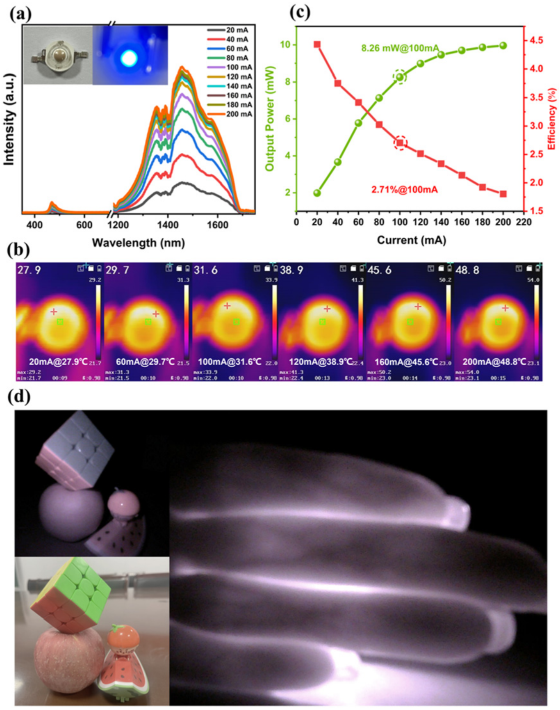

Fig. 4 (a) EL spectra. (b) Thermographs of the device at different driven currents from 20 to 200 mA. (c) Output optical powers and conversion efficiencies of the NIR-II pc-LED depending on the driving current. (d) Photographs were obtained under fluorescent light and NIR-II light, respectively.

blue light into NIR light. In addition, when the driving current is increased from 20 to 200 mA, the PL intensity gradually increases. At the same time, the operating temperature of the NIR pc-LED device increased from 28 °C to 49 °C, as induced by the heat buildup that occurs with higher drive currents (Fig. 4b). Such a small temperature change is acceptable in applications. Fig. 4c shows the relationship between NIR-II output power and photoelectric conversion efficiency of the NIR-II pc-LED as a function of driving current. Moreover, with an increase in the drive current from 10 to 200 mA, the output power of the prepared NIR-II pc-LED escalates from 1.98 to 9.96 mW, while the photoelectric conversion efficiency shows the opposite trend from 4.43 to 1.81%. The primary cause of this phenomenon is the efficiency drop of the blue light chip.[23] Under the illumination of the NIR-II pc-LED light source in darkness, the NIR-II camera is able to capture shapes and positions of fruits and toys, as well as finger veins (Fig. 4d). This fully demonstrates the potential applications of the prepared NIR-II pc-LED in night vision and medical imaging.

To further demonstrate that the fabricated NIR-II pc-LED can be applied to non-destructive testing, a spectral experimental setup is shown in Fig. 5a. Fig. 5b displays the absorption spectra of four frequently used organic solvents, which include H_2O, C_2H_5OH, $C_4H_{10}O$, and $C_6H_{14}O$. Interestingly, NIR-II PL spectra can cover more information about the molecule and contribute to higher detection sensitivity compared to the NIR-I PL spectra. There are characteristic absorption bands toward the NIR-II region for four solvents, such as H_2O (~1390 nm), C_2H_5OH (~1185 and ~1585 nm), $C_4H_{10}O$ (~1195 and ~1595 nm), $C_6H_{14}O$ (~1210 and ~1595 nm). Chemical analysis was performed using the original PL spectrum of $LZSO:0.03Cr^{3+},0.03Ni^{2+}$ and the PL spectrum of NIR light penetrating different solvents (Fig. 5c). Therefore, the setup can distinguish differences between solvents by detecting the PL intensity and peak position.

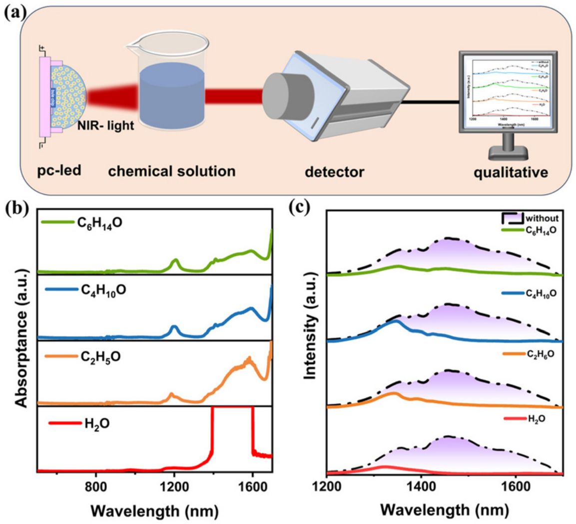

Fig. 5 (a) Schematic diagram of NIR spectral analysis device. (b) Measured absorption spectra of 4 organic solvents including H_2O, C_2H_5OH, $C_4H_{10}O$, and $C_6H_{14}O$. (c) Spectra of NIR-II from $LZSO:0.03Cr^{3+},0.03Ni^{2+}$ before (black dotted line) and after (solid line) penetrating different organic solvents.

4 Conclusions

To summarize, we synthesized a novel Cr^{3+}–Ni^{2+} co-doped LZSO phosphor using a conventional high-temperature solid-phase method. The prepared $LZSO:Cr^{3+},Ni^{2+}$ phosphor utilizes the sensitization effect of Cr^{3+} ions on the Ni^{2+}, achieving blue-light excitation and efficient broadband emission in the NIR-II region. The obtained $LZSO:Cr^{3+},Ni^{2+}$ exhibited broadband emission peaking at 1465 nm, with a large FWHM of 300 nm and an IQE of 43.3% under 426 nm excitation. More intriguingly, using the prepared NIR-II pc-LED as the light source for night vision, medical imaging, and non-destructive analysis were realized. Furthermore, the phosphor has the characteristics of ultra-wideband emission with dual emission peaks in the NIR-I and NIR-II regions, as well as high sensitivity, which hold promise for the application of NIR thermometry in biotechnology. This research not only obtains a prospective phosphor for future NIR-II light sources but also highlights the vast application prospects of NIR technology.

Author contributions

Zhexuan Gao: investigation, visualization, methodology, formal analysis, writing – original draft. Yi Zhang: supervision, formal analysis. Yinyan Li: investigation, validation. Peng Zhang: formal analysis. Xiaolong Dong: formal analysis. Shilong Zhao: investigation, conceptualization. Degang Deng: conceptualization, writing – review and editing, funding acquisition. Shiqing Xu: methodology, formal analysis.

Conflicts of interest

There are no conflicts to declare.

Acknowledgements

This research is supported by Zhejiang Provincial Natural Science Foundation of China (Grant No. LZ22F050002), National Key Research and Development Program of China (SQ2023YFE0201285), National Natural Science Foundation of China (62075205) and Zhejiang Provincial Key Research and Development Program (Grant No. 2021C01027, 2021C01024 and 2022C01133).

References

1 F. Zhao, Z. Song and Q. Liu, Advances in Chromium–Activated Phosphors for Near–Infrared Light Sources, *Laser Photonics Rev.*, 2022, **16**, 2200380.

2 Q. Pang, Y. Wang, L. Yan, G. Zhu, S. Xu, J. Zhang, X. Zhang, Y. Cao and B. Chen, Cr^{3+}-Cr^{3+} Ion Pair Induced Fast Energy Migration in Cr^{3+} Doped Na-β-Al_2O_3 Ultra-Wide Near-Infrared Phosphors for NIR Spectroscopy Application, *Laser Photonics Rev.*, 2024, **18**, 2301039.

3 T. Yang, L. Chu, Y. Qin, Q. Zhou, J. Wan, H. Tang, Y. Ye and Z. Wang, An efficient and thermally stable source with Cr^{3+} near-infrared luminescence for non-destructive testing applications, *Mater. Today Chem.*, 2024, **35**, 101918.

4 M. Zhao, S. Liu, H. Cai, F. Zhao, Z. Song and Q. Liu, Cr^{3+}-Doped double perovskite antimonates: efficient and tunable phosphors from NIR-I to NIR-II, *Inorg. Chem. Front.*, 2022, **9**, 4602–4607.

5 M. Xu, Z. Li, Q. Li, T. Mou, X. Wang, D. Yan, Y. Li, X. Zhou, Z. Fang and L. Ning, Thermally Stable NIR Emission from Disordered $Ba_5La_3MgAl_3O_{15}$:Cr^{3+} with Peak Wavelength Beyond 900 nm, *Adv. Opt. Mater.*, 2024, 2303144, DOI: 10.1002/adom.202303144.

6 S. Wei, Z. Lyu, D. Sun, S. Shen, X. Zhang, Z. Lu, P. Luo, H. Hu and H. You, A NIR phosphor with ultra-broadband emission enabled by dual energy transfer within two Cr^{3+} emitters and $Cr^{3+} \rightarrow Yb^{3+}$, *J. Mater. Chem. C*, 2024, **12**, 4977–4985.

7 X. Wang, Z. Wang, J. Cui, Y. Yao, M. Zheng, M. Zhang, L. Cao, Z. Yang, H. Suo and P. Li, Multifunctional Near-Infrared (NIR) Phosphors with NIR I and NIR II Luminescence for Biological Detection, *ACS Appl. Electron. Mater.*, 2021, **4**, 432–442.

8 A. Satpathy, W. T. Huang, M. H. Chan, T. Y. Su, M. Kamiński, N. Majewska, S. Mahlik, G. Leniec, S. M. Kaczmarek, M. Hsiao and R. S. Liu, Near–Infrared I/II Nanophosphors with Cr^{3+}/Ni^{2+} Energy Transfer for Bioimaging, *Adv. Opt. Mater.*, 2023, **11**, 2300321.

9 L. Jiang, L. Zhang, X. Jiang, J. Xie, G. Lv and Y. Su, Cr^{3+}–Yb^{3+}–Ni^{2+} Tri–Doped NIR Phosphors with Spectral Output Covering NIR–I and NIR–II Regions, *Adv. Mater. Technol.*, 2024, **9**, 2301495.

10 B. M. Liu, X. X. Guo, L. Huang, R. F. Zhou, R. Zou, C. G. Ma and J. Wang, A Super–Broadband NIR Dual–Emitting Mg_2SnO_4:Cr^{3+},Ni^{2+} Phosphor for Ratiometric Phosphor–Converted NIR Light Source Applications, *Adv. Mater. Technol.*, 2023, **8**, 2201181.

11 L. Yuan, Y. Jin, D. Zhu, Z. Mou, G. Xie and Y. Hu, Ni^{2+}-Doped Yttrium Aluminum Gallium Garnet Phosphors: Bandgap Engineering for Broad-Band Wavelength-Tunable Shortwave-Infrared Long-Persistent Luminescence and Photochromism, *ACS Sustainable Chem. Eng.*, 2020, **8**, 6543–6550.

12 M. Lin, Z. Gao, C. Xu, Y. Yuan, Y. Tang, T. Liu and L. Sun, Enhanced and Broadened NIR Emission of $CaZnGe_2O_6$:Cr^{3+} by Yb^{3+} Codoping for NIR Applications, *ACS Appl. Opt. Mater.*, 2023, **1**, 724–735.

13 L. Jiang, L. Zhang, X. Zhao, X. Jiang, P. Gao and Y. Su, Awakening the Dumb Site to Realize Ultra–Broadband NIR Phosphor, *Laser Photonics Rev.*, 2024, **18**, 2301226.

14 J. Wang, X. Han, Y. Zhou, Z. Wu, D. Liu, C. Zeng, S. Cao and B. Zou, Ion Substitution Strategy toward High-Efficiency Near-Infrared Photoluminescence of $Cs_2KIn_{1-y}Al_yF_6$:Cr^{3+} Solid Solutions, *J. Phys. Chem. Lett.*, 2023, **14**, 1371–1378.

15 Q. Zhang, X. Wei, J. Zhou, B. Milićević, L. Lin, J. Huo, J. Li, H. Ni and Z. Xia, Thermal Stability Improvement of Cr^{3+}–Activated Broadband Near–Infrared Phosphors via State Population Optimization, *Adv. Opt. Mater.*, 2023, **11**, 2300310.

16 Z. Jia, C. Yuan, Y. Liu, X.-J. Wang, P. Sun, L. Wang, H. Jiang and J. Jiang, Strategies to approach high performance in Cr^{3+}-doped phosphors for high-power NIR-LED light sources, *Light: Sci. Appl.*, 2020, **9**, 86.

17 C.-Y. Peng, B. Wang, L.-F. Yuan, K.-G. Hu, G. Chen, H.-Y. Wu, Y.-H. Hu and Y.-H. Jin, Six- and five-coordinated Cr^{3+} in Ga2GeO5 invokes tunable broadband near-infrared emission toward night-vision applications, *Rare Met.*, 2023, **42**, 3787–3796.

18 S. Chen, M. Han, J. Li, Y. Li, Z. Gao, Y. Zhang, M. Meng, Q. Zhang, D. Deng and L. Chen, Cr^{3+}-activated $NaInSi_2O_6$: An efficient broadband near-infrared phosphor with its applications in LED, *Ceram. Int.*, 2023, **49**, 36360–36367.

19 S. Miao, Y. Liang, Y. Zhang, D. Chen and X.-J. Wang, Broadband Short-Wave Infrared Light-Emitting Diodes Based on Cr^{3+}-Doped $LiScGeO_4$ Phosphor, *ACS Appl. Mater. Interfaces*, 2021, **13**, 36011–36019.

20 G.-H. Li, J.-B. Huang, Q.-H. Yang, J. Wang, G.-M. Cai and X.-J. Wang, Composition–structure–luminescence and enhancement of Cr^{3+} activated broadband near infrared phosphors for night vision, bio-imaging, and noninvasive detection, *J. Mater. Chem. C*, 2023, **11**, 16578–16586.

21 L. Yao, Q. Shao, S. Han, C. Liang, J. He and J. Jiang, Enhancing Near-Infrared Photoluminescence Intensity and Spectral Properties in Yb^{3+} Codoped $LiScP_2O_7$:Cr^{3+}, *Chem. Mater.*, 2020, **32**, 2430–2439.

22 Z. Lu, S. Chen, Y. Liu, C. Yuan, R. Li, P. Sun, Z. Luo, Z. Liu and J. Jiang, $LiGaP_2O_7$:Cr^{3+}, Yb^{3+} phosphors for broadband NIR LEDs toward multiple applications, *J. Alloys Compd.*, 2023, **956**, 170311.

23 G. Liu, T. Hu, M. S. Molokeev and Z. Xia, Li/Na substitution and Yb^{3+} co-doping enabling tunable near-infrared emission in $LiIn_2SbO_6$:Cr^{3+} phosphors for light-emitting diodes, *iScience*, 2021, **24**, 102250.

24 Y. Zhang, S. Miao, Y. Liang, C. Liang, D. Chen, X. Shan, K. Sun and X.-J. Wang, Blue LED-pumped intense short-wave infrared luminescence based on Cr^{3+}-Yb^{3+}-co-doped phosphors, *Light: Sci. Appl.*, 2022, **11**, 136.

25 R. Shi, S. Miao, X. Lv, D. Chen, Y. Zhang and Y. Liang, High–Efficiency Short–Wave Infrared Emitter Enabled by

Cr^{3+}–Yb^{3+} Co–Doped Phosphor, *Adv. Opt. Mater.*, 2024, 2303221, DOI: **10.1002/adom.202303221**.

26 Q. Jia, L. Yao, S. Yu, S. Gong, J. Jiang and Q. Shao, Efficient and ultra-broadband Cr^{3+}/Ni^{2+} co-doped phosphors for light-emitting diodes with spectral output over NIR-I and NIR-II regions, *J. Mater. Chem. C*, 2023, **11**, 11046–11054.

27 S. Miao, Y. Liang, R. Shi, W. Wang, Y. Li and X.-J. Wang, Broadband Short-Wave Infrared-Emitting $MgGa_2O_4$:Cr^{3+}, Ni^{2+} Phosphor with Near-Unity Internal Quantum Efficiency and High Thermal Stability for Light-Emitting Diode Applications, *ACS Appl. Mater. Interfaces*, 2023, **15**, 32580–32588.

28 J. Chen, Y. Gao, J. Chen, X. Lu, M. Tan and J. Qiu, Designing and controlling the Ni^{2+}-activated (Zn,Mg)Al_2O_4 spinel solid-solution for phosphor-converted broadband near-infrared illumination, *J. Mater. Chem. C*, 2023, **11**, 2217–2228.

29 M. Jin, F. Li, J. Xiahou, L. Zhu, Q. Zhu and J.-G. Li, A new persistent luminescence phosphor of $ZnGa_2O_4$:Ni^{2+} for the second near-infrared transparency window, *J. Alloys Compd.*, 2023, **931**, 167491.

30 S. Miao, Y. Liang, Y. Zhang, D. Chen and X. J. Wang, Blue LED–Pumped Broadband Short–Wave Infrared Emitter Based on $LiMgPO_4$:Cr^{3+},Ni^{2+} Phosphor, *Adv. Mater. Technol.*, 2022, **7**, 2200320.

31 Q. Zhang, G. Li, G. Li, D. Liu, P. Dang, L. Qiu, H. Lian, M. S. Molokeev and J. Lin, Optical Thermometer Based on Efficient Near–Infrared Dual–Emission of Cr^{3+} and Ni^{2+} in Magnetoplumbite Structure, *Adv. Opt. Mater.*, 2023, **12**, 2301429.

32 M. Han, S. Chen, J. Li, Z. Gao, Y. Zhang, Y. Shen, Y. Tian and D. Deng, Sr_2(Ga/Al)TaO_6:Cr^{3+} phosphor with tunable near-infrared emitting for light-emitting diodes and optical thermometer, *J. Alloys Compd.*, 2024, **973**, 172927.

33 D. Kovacheva, T. Trendafilova, K. Petrov and A. Hewat, Cation ordering in $Li_2M(II)Sn_3O_8$,M(II)=Mn,Zn, *J. Solid State Chem.*, 2002, **169**, 44–52.

34 S. Qing, J. Wan, T. Yang, Q. Zhou, Y. Zhou, Z. Wang, D. Wen and M. Wu, Rational design for broad near-infrared emission from a two-sited Rb_2LiAlF_6:Cr^{3+} phosphor with high efficiency and thermal stability for spectroscopic applications, *Inorg. Chem. Front.*, 2024, **11**, 2718–2725.

35 Z. Lu, Y. Liu, S. Chen, P. Sun, Z. Luo, X.-J. Wang and J. Jiang, Improved Near-Infrared Luminescence Properties of $LiScSi_2O_6$:Cr^{3+},Yb^{3+} Phosphors via Efficient Energy Transfer, *ACS Appl. Opt. Mater.*, 2023, **1**, 1097–1103.

36 T. Suzuki, G. S. Murugan and Y. J. J. O. L. Ohishi, Spectroscopic properties of a novel near-infrared tunable laser material Ni : $MgGa_2O_4$, *J. Lumin.*, 2005, **113**, 265–270.

37 Y. Zhang, Z. Gao, Y. Li, S. Chen, M. Han, J. Li, Q. Zhang, Y. Shen, D. Deng and S. Xu, Broadband La_2LiSbO_6: Cr^{3+} Phosphors with Double Luminescent Centers for NIR pc-LEDs, *Inorg. Chem.*, 2023, **62**, 17371–17381.

38 Z. Song, P. A. Tanner and Q. Liu, Host Dependency of Boundary between Strong and Weak Crystal Field Strength of Cr^{3+} Luminescence, *J. Phys. Chem. Lett.*, 2024, **15**, 2319–2324.

39 H. Zhang, J. Zhong, F. Du, L. Chen, X. Zhang, Z. Mu and W. Zhao, Efficient and Thermally Stable Broad-Band Near-Infrared Emission in a $KAlP_2O_7$:Cr^{3+} Phosphor for Nondestructive Examination, *ACS Appl. Mater. Interfaces*, 2022, **14**, 11663–11671.

40 C. Wang, Y. Zhang, X. Han, D. Hu, D. He, X. Wang and H. Jiao, Energy transfer enhanced broadband near-infrared phosphors: Cr^{3+}/Ni^{2+} activated $ZnGa_2O_4$–Zn_2SnO_4 solid solutions for the second NIR window imaging, *J. Mater. Chem. C*, 2021, **9**, 4583–4590.

41 Q. Zhang, D. Liu, Z. Wang, P. Dang, H. Lian, G. Li and J. Lin, $LaMgGa_{11}O_{19}$:Cr^{3+},Ni^{2+} as Blue–Light Excitable Near–Infrared Luminescent Materials with Ultra–Wide Emission and High External Quantum Efficiency, *Adv. Opt. Mater.*, 2023, **11**, 2202478.

42 Y. Wang, M. Shang, S. Huang, Y. Sun, Y. Zhu, X. Xing, P. Dang and J. Lin, Continuous Ultra–Broadband Near–Infrared Sc_2O_3–Based Nanophosphor Realized by Spectral Bridge of Cr^{3+}–Yb^{3+}–Cr^{4+} for Multiple Optical Applications, *Adv. Opt. Mater.*, 2023, **11**, 2300517.

43 Y. Wang, M. Shang, Y. Sun, Y. Zhu, X. Xing, P. Dang and J. Lin, Small Stokes Shift and Two–Site Occupation in the ANb_2O_6:Cr^{3+} (A = Zn/Mg) Phosphors Toward Highly Efficient Ultra–Broadband Near–Infrared Emission for Multifunctional Applications, *Adv. Opt. Mater.*, 2023, **12**, 2302611.

44 S. Wang, Z. Lyu, D. Sun, S. Shen and H. You, Tailoring the Cr^{3+} Emission via Combinatorial Management of Crystal–Field and Energy Transfer for Multiple NIR LEDs, *Adv. Opt. Mater.*, 2024, 2303140, DOI: **10.1002/adom.202303140**.

45 Y. Zhuo, F. Wu, Y. Niu, Y. Wang, Q. Zhang, Y. Teng, H. Dong and Z. Mu, Super Broadband Emission Across NIR–I and NIR–II Under Blue Light Excitation of Cr^{3+}, Ni^{2+} Co–Doped Sr_2GaTaO_6 Phosphor Achieved by Two–Site Occupation and Effective Energy Transfer, *Laser Photonics Rev.*, 2024, 2400105, DOI: **10.1002/lpor.202400105**.

46 M. U. Dumesso, W. Xiao, G. Zheng, E. T. Basore, M. Tang, X. Liu and J. Qiu, Efficient, Stable, and Ultra–Broadband Near–Infrared Garnet Phosphors for Miniaturized Optical Applications, *Adv. Opt. Mater.*, 2022, **10**, 2200676.

47 W.-T. Huang, V. Rajendran, M.-H. Chan, M. Hsiao, H. Chang and R.-S. Liu, Near-Infrared Windows I and II Phosphors for Theranostic Applications: Spectroscopy, Bioimaging, and Light-Emitting Diode Photobiomodulation, *Adv. Opt. Mater.*, 2023, **11**, 2202061.

48 R. Shi, S. Miao, Y. Zhang, X. Lv, D. Chen and Y. Liang, Blue-light-excitable pure and efficient short-wave infrared luminescence via Cr^{3+} → Yb^{3+} energy transfer in a $KYbP_2O_7$:Cr^{3+} phosphor, *J. Mater. Chem. C*, 2023, **11**, 2748–2755.

49 Z. Chen, S. Du, K. Zhu, Z. Tian, J. Zhang, F. Li, S. Zhang, S. Zhao, W. Cui, X. Yuan, K. Chen, G. Yuan and G. Liu, Mn^{4+}-Activated Double-Perovskite-Type Sr_2LuNbO_6 Multifunctional Phosphor for Optical Probing and

Lighting, *ACS Appl. Mater. Interfaces*, 2023, **15**, 28193–28203.

50 M. Back, J. Ueda, H. Nambu, M. Fujita, A. Yamamoto, H. Yoshida, H. Tanaka, M. G. Brik and S. Tanabe, Boltzmann Thermometry in Cr^{3+}–Doped Ga_2O_3 Polymorphs: The Structure!. Matters, *Adv. Opt. Mater.*, 2021, **9**, 2100033.

51 K. Elzbieciak-Piecka and L. Marciniak, Optical heating and luminescence thermometry combined in a Cr^{3+}-doped $YAl_3(BO_3)_4$, *Sci. Rep.*, 2022, **12**, 16364.

52 Y. Huo, H. Cai, Y. Shao, Z. Song and Q. Liu, Enabling Yb^{3+} Luminescence with Visible Light Response in Mg_2GeO_4 via Energy Transfer, *Inorg. Chem.*, 2023, **62**, 14402–14410.

53 Q. Wang, S. Wang, R. Pang, T. Tan, T. Tan, H. Wen, S. Zhang, H. You, C. Li and H. Zhang, Two-site occupation in Cr^{3+}-activated $BaIn_2(P_2O_7)_2$ phosphor for broadband near-infrared thermometry and LED applications, *Mater. Res. Bull.*, 2023, **163**, 112222.